Received: 17 April 2023 | Revised: 11 September 2023 | Accepted: 28 September 2023

DOI: 10.1002/cey2.486

RESEARCH ARTICLE

CARBON ENERGY WILEY

Small but mighty: Empowering sodium/potassium-ion battery performance with S-doped SnO_2 quantum dots embedded in N, S codoped carbon fiber network

Shengnan He[1] | **Hui Wu**[2] | **Shuang Li**[2,3] | **Ke Liu**[4] | **Yaxiong Yang**[1] | **Hongge Pan**[1] | **Xuebin Yu**[2]

[1]Institute of Science and Technology for New Energy, Xi'an Technological University, Xi'an, China

[2]Department of Materials Science, Fudan University, Shanghai, China

[3]Wanxiang A123 Systems Corporation, Hangzhou, China

[4]School of Material Science and Engineering, Shanghai University, Shanghai, China

Correspondence
Yaxiong Yang, Institute of Science and Technology for New Energy, Xi'an Technological University, 710021 Xi'an, China.
Email: yangyaxiong@xatu.edu.cn

Hui Wu and Xuebin Yu, Department of Materials Science, Fudan University, 200433 Shanghai, China.
Email: luoshi2010@yeah.net and yuxuebin@fudan.edu.cn

Funding information
National Natural Science Foundation of China, Grant/Award Number: 51971065; Innovation Program of Shanghai Municipal Education Commission, Grant/Award Number: 2019-01-07-00-07-E00028

Abstract

SnO_2 has been extensively investigated as an anode material for sodium-ion batteries (SIBs) and potassium-ion batteries (PIBs) due to its high Na/K storage capacity, high abundance, and low toxicity. However, the sluggish reaction kinetics, low electronic conductivity, and large volume changes during charge and discharge hinder the practical applications of SnO_2-based electrodes for SIBs and PIBs. Engineering rational structures with fast charge/ion transfer and robust stability is important to overcoming these challenges. Herein, S-doped SnO_2 (S–SnO_2) quantum dots (QDs) (≈3 nm) encapsulated in an N, S codoped carbon fiber networks (S–SnO_2–CFN) are rationally fabricated using a sequential freeze-drying, calcination, and S-doping strategy. Experimental analysis and density functional theory calculations reveal that the integration of S–SnO_2 QDs with N, S codoped carbon fiber network remarkably decreases the adsorption energies of Na/K atoms in the interlayer of SnO_2–CFN, and the S doping can increase the conductivity of SnO_2, thereby enhancing the ion transfer kinetics. The synergistic interaction between S–SnO_2 QDs and N, S codoped carbon fiber network results in a composite with fast Na^+/K^+ storage and extraordinary long-term cyclability. Specifically, the S–SnO_2–CFN delivers high rate capacities of 141.0 mAh g^{-1} at 20 A g^{-1} in SIBs and 102.8 mAh g^{-1} at 10 A g^{-1} in PIBs. Impressively, it delivers ultra-stable sodium storage up to 10,000 cycles at 5 A g^{-1} and potassium storage up to 5000 cycles at 2 A g^{-1}. This study provides insights into constructing metal oxide-based carbon fiber network structures for high-performance electrochemical energy storage and conversion devices.

KEYWORDS
carbon fiber network, heteroatom doping, potassium-ion battery, sodium-ion battery, S–SnO_2 quantum dot

Shengnan He, Hui Wu, and Shuang Li contributed equally to this work.

1 | INTRODUCTION

In recent decades, lithium-ion batteries (LIBs) have been playing a crucial role in the field of electrochemical energy storage systems owing to their exceptional advantages, such as high open circuit voltage, high energy density, and long-term cycling life.[1–3] However, the scarcity and uneven distribution of lithium resources hamper the sustainable development of LIBs.[4] As a result, sodium-ion batteries (SIBs) and potassium-ion batteries (PIBs) have emerged as potential alternatives to LIBs, given that sodium and potassium are widely available and exhibit similar electrochemical behavior to that of LIBs.[3] However, the larger radius of Na/K ions (1.02/1.38 Å) compared to Li^+ (0.76 Å) makes it more challenging for them to insert into anode materials, leading to a lower reversible capacity.[5] Therefore, developing suitable electrode materials for SIBs and PIBs with large reversible capacities, superior cycling stability, and high-rate performance is highly desirable.[6,7]

Much effort has been devoted to finding suitable anode materials to improve the electrochemical performance of SIBs and PIBs.[8–10] Among potential anode materials, tin oxide (SnO_2) stands out due to its high theoretical capacity (782 mAh g^{-1}), abundance, low cost, and environmental friendliness.[11,12] However, SnO_2 suffers from significant volume changes (~300%) induced by alloying/dealloying reactions, leading to severe pulverization and aggregation, unstable solid electrolyte interphase (SEI), and effective electrical contact loss, resulting in inferior electrochemical performance.[13,14] One effective approach to address these drawbacks is to reduce the size of SnO_2 particles to nanometer size or even to the quantum size ($d < 10$ nm), which can better accommodate the absolute volume change and offer more active sites for adsorption, thus enhancing electrochemical performance.[15] Moreover, it has also been identified that smaller particles have shorter path lengths for ion transport and faster ion mobility, especially at high rates.[16] However, as the particle size decreases, the increasingly large specific area and interfaces between SnO_2 and electrolyte could lead to the formation of unstable SEI film and aggregation of particles during cycling, thus leading to inferior electrochemical performance. To overcome the side reactions, integrating SnO_2 particles with carbon, especially composited SnO_2 with well-designed carbon architecture, would be a potential approach that has been demonstrated as an effective electrode configuration. The introduction of carbonaceous materials with a well-designed structure can not only enhance the conductivity of composites but also maintain integrity stability to prevent the aggregation of active particles during cycling.[17] For example, Qiu et al.[11] fabricated SnO_2 nanoparticles anchored on N-doped carbon foam as PIBs anode, which delivered enhanced cycling stability over 400 cycles at 1 A g^{-1}. Furthermore, as it is widely recognized, the low electrical conductivity of SnO_2 anode materials poses another severe challenge, leading to slow ion/electron transfer and ultimately impacting the rate performance.[14] Although the compositing of carbon can enhance the conductivity of the resulting composites, it does not modify the intrinsic conductivity of SnO_2. Therefore, it is imperative to further enhance the electrochemical performance of SnO_2-based anodes by improving the inherent conductivity of SnO_2. Doping SnO_2 with exotic atoms at the atomic level is a promising approach to effectively modify its electrical properties.[18] For instance, Sb-doped SnO_2/graphene-carbon nanotube aerogels designed by Kim for SIBs exhibited enhanced ion transfer kinetics due to increased conductivity of SnO_2 particles resulting from Sb doping, and the composite maintained 74% of its capacity at 1 A g^{-1} after 500 cycles.[18] Moreover, doping carbon with exotic atoms such as N and S can further improve the electronic conductivity of the composite and provide more reversible active sites for potassium/sodium ion storage.[19] Therefore, nonmetal heteroatom doping (e.g., N, P, and S) is the optimal choice for simultaneously improving the electronic conductivity of SnO_2 and the carbon matrix. Considering all the aforementioned factors, an optimal approach to achieve high electrochemical performance for SnO_2-based anode materials would involve the combination of ultrasmall SnO_2 particles with heteroatom doping, along with a modified conductive carbon matrix having a well-designed structure.

Herein, we found an opportunity to prepare highly conducting SnO_2 composites by combining the S–SnO_2 quantum dots (QDs) and the N, S codoped carbon fiber networks (CFN) to effectively improve the electrochemical performance of SnO_2. In addition to the benefits of the carbon matrix mentioned above, incorporating the carbon fiber network structure could provide numerous ion/electron transport channels and internal void space between fibers, thereby further improving the electrochemical performance of the SnO_2-based anode. In this work, the S–SnO_2 QDs (≈3 nm) encapsulated in N, S codoped carbon fiber networks (denoted as S–SnO_2–CFN) were easily prepared using sequential freeze-drying, calcination, and S-doping strategy. The freeze-drying method plays a critical role in controlling the morphology of the final product, as it leads to the formation of Sn–chitosan sol-gel hybrid materials. Incorporating S–SnO_2 QDs can reduce absolute volume change, decrease ion diffusion length, and improve electrical conductivity. The relatively weaker Sn–S bonds

in S–SnO_2 QDs compared to Sn–O bonds in SnO_2 are also beneficial for Na^+/K^+ insertion/extraction processes. Additionally, the N, S codoped carbon fiber network structure can enhance electronic conductivity, provide abundant active sites and electron/ion transport channels, and produce internal void spaces between fibers to accommodate volume expansion. Density functional theory (DFT) calculations further confirmed that the integration of SnO_2 with N, S codoped carbon fiber network can significantly decrease the adsorbed energies of Na/K atoms in the interlayer of SnO_2–CFN and S doping can increase the conductivity of SnO_2, thereby enhancing ion transfer kinetics. These advantages of the S–SnO_2–CFN composite synergistically contribute to its exceptional performance in sodium and potassium storage. Specifically, the S–SnO_2–CFN anode exhibits remarkable sodium storage performance in both long-term cyclability and rate capability, exhibiting a stable capacity of 237.0 mAh g^{-1} at 5 A g^{-1} after 10,000 cycles and a high rate capacity of 141.0 mAh g^{-1} at 20 A g^{-1}. Furthermore, as an anode for PIBs, the S–SnO_2–CFN anode delivers impressive potassium performance, with a stable capacity of 145.5 mAh g^{-1} at 2 A g^{-1} after 5000 cycles and a high rate capacity of 102.8 mAh g^{-1} at 20 A g^{-1}.

2 | EXPERIMENTAL SECTION

2.1 | Chemical

The following chemicals were used without further purification. The raw materials of tin(II) chloride dihydrate ($SnCl_2{\cdot}2H_2O$, 98%; ACS reagent), chitosan ($[C_6H_{11}NO_4]_n$, medium molecular weight), and sulfur (S, 99.99%) were all purchased from Sinopharm Chemical Reagent Co., Ltd. Tin oxide (SnO_2, 99.5%) was purchased from Aladdin Ltd.

2.2 | Material preparation

In a typical synthesis, 0.33 g of chitosan powder was dissolved in 100 mL of an acetic acid solution, followed by the slow addition of a $SnCl_2{\cdot}2H_2O$ solution in water (1 g in 5 mL) while stirring magnetically. After stirring for 1 h, the mixed solution was rapidly frozen using liquid nitrogen and then subjected to a freezing-dry process. The resulting Sn–chitosan powder was then pyrolyzed in an argon atmosphere at 500°C for 4 h to form the SnO_2–CFN-2 composite. Subsequently, the S-doped SnO_2–CFN composite (referred to as S–SnO_2–CFN-2) was obtained by further annealing the SnO_2–CFN composite with sulfur powder (1:2 in weight ratio) at 450°C with a heating rate of 2°C/min for 3 h under an argon atmosphere. For comparison, different S–SnO_2–CFN composites were synthesized using the same conditions with 0.165 g (S–SnO_2–CFN-1) and 0.66 g (S–SnO_2–CFN-3) of chitosan.

2.3 | Materials characterization

The morphology and microstructure were examined using a field emission scanning electron microscope (FESEM, JEOL7500FA) and transmission electron microscope (TEM, JEOL JEM-2011) coupled with an energy dispersive X-ray spectrometer (EDS). The crystal structure and composition were characterized by X-ray diffraction (XRD) with a Bruker D8 advanced diffractometer using Cu Kα ($\lambda = 1.5406$ Å) radiation (D8 Advance; Bruker AXS). Raman spectra were recorded using a LabRam HR800 Raman microscope (HR800; Horiba Scientific). Fourier-transform infrared spectroscopy (FTIR) spectra were obtained on a Nicolet iS50 FTIR spectrometer. The X-ray photoelectron spectrometer (XPS) data were collected using a Thermo Scientific K-Alpha XPS system (Thermo Fisher Scientific) with a microfocused monochromatic Al Kα X-ray source (1486.6 eV). The content of S in the composites was analyzed using inductively coupled plasma-mass spectrometry (ICP-MS; PerkinElmer NexION 300X).

2.4 | Electrochemical characterization

The working electrode was fabricated by first preparing a slurry consisting of the as-synthesized samples (70 wt%), carboxymethyl cellulose (20 wt%), and super P (10 wt%) in water, which was then coated on a copper foil and dried overnight in a vacuum oven at 80°C to achieve a mass of active materials of approximately 0.7−1.0 mg cm^{-2}. Electrochemical properties were measured using CR2032-type coin cells assembled in an N_2-filled glovebox. Glass fiber membrane served as the separator, and metallic sodium and potassium were employed as the counter electrodes for SIBs and PIBs, respectively. For SIBs, the electrolyte used was a 1 M $NaClO_4$ solution in ethylene carbonate (EC)/diethyl carbonate (DEC) (1:1 volumetric ratio) with 10 vol% fluoroethylene carbonate added as an additive. In contrast, a solution of 0.8 M KPF_6 in EC and DEC (1:1 volume ratio) was utilized as the electrolyte for PIBs. Cyclic voltammetry (CV) tests were performed on a CHI 660D electrochemical workstation within a potential range of 0.01–3 V for both SIBs and PIBs. Galvanostatic discharge and charge (GDC)

measurements were carried out using the NETWARE BTS-5V battery test system.

2.5 | Computational methods

All DFT calculations in this study were performed within the generalized gradient approximation using the Perdew–Burke–Ernzerhof formulation using the projector augmented wave.[20–24] Partial occupancies of the Kohn–Sham orbitals were allowed using the Gaussian smearing method and a width of 0.05 eV. The $2 \times 2 \times 1$ Monkhorst–Pack k-points and 450 eV of cut-off energy were used to optimize the surface of SnO_2(110) and interface structure. The vacuum spacing in a direction perpendicular to the plane of the structure is 20 Å for the surfaces. The electronic energy was considered self-consistent when the energy change was smaller than 10^{-5} eV. A geometry optimization was considered convergent when the energy change was smaller than 0.05 eV Å^{-1}. Finally, all adsorption energies (E_{ads}) were calculated by the equation: $E_{ads} = E_{ad/sub} - E_{ad} - E_{sub}$, where $E_{ad/sub}$, E_{ad}, and E_{sub} are the total energies of the optimized adsorbate/substrate system, the adsorbate in the structure, and the clean substrate, respectively.

3 | RESULTS AND DISCUSSION

Figure 1A presents the schematic illustration of the preparation process for the S–SnO_2–CFN carbon fibers network. Initially, the Sn–chitosan fiber composite was fabricated by the sol-gel polymerization of ubiquitous chitosan and $SnCl_2{\cdot}2H_2O$, followed by a freeze-drying process. The dissolved chitosan can be crosslinked by metal salt solutions (Sn^{2+}), resulting in the separated molecular chains assembled in parallel to form crosslinked Sn–chitosan nanofibers. Subsequently, the intermediate product of the SnO_2–CFN composite was achieved by annealing the Sn–chitosan composite under an Ar atmosphere. Finally, the sulfidation method was used to transform the intermediate product into S–SnO_2–CFN composites. The morphologies and structural details of as-prepared S–SnO_2–CFN samples were characterized by FESEM, TEM, and high-resolution TEM (HRTEM). Figure 1B,E shows scanning electron microscopy (SEM) images of S–SnO_2–CFN-1. It can be observed that some carbon fibers were formed along with some particles of irregular shape and size after the sulfidation process. When the amount of chitosan increased to 0.33 g, the S–SnO_2–CFN-2 displayed a well-designed crosslinked fiber structure with an average diameter of 100 nm (Figure 1C,F). When the amount of chitosan continues to increase to 0.66 g, it can be found that although some carbon fibers are formed, there are still many particles with a diameter of about 500 nm (Figure 1D,G). This result shows that the morphology of the product can be controlled by controlling the amount of chitosan added, which could be assigned to the coupling interactions between Sn^{2+} and chitosan. It is well known that a carbon fiber network with abundant surface areas is beneficial for facilitating electron/ion transport, thus enhancing the electrochemical performance. Moreover, the morphologies of SnO_2–CFN–2 and pure SnO_2 were also characterized, as shown in Figures S1 and S2, in which they display crosslinked fiber network structures and quasi-spherical structures, respectively. Moreover, to gain further insight into the microstructure of S–SnO_2–CFN-2, the TEM measurement was carried out, as presented in Figure 1H,I. It can be seen that the S–SnO_2–CFN-2 shows relatively smooth surfaces with crosslinked network structures. The S–SnO_2 QDs are uniformly and densely distributed along the fibers. Moreover, the size distribution inserted in Figure 1I shows a narrow size distribution of SnO_2 QDs with a mean size of 3 nm. Benefitting from the well-controlled synthesis procedure, the uniform dispersed S–SnO_2 particles can tightly embed in carbon fibers instead of adsorb physically, which can prevent the S–SnO_2 particles from falling off during repeated charging and discharging process. The HRTEM image (Figure 1J) illustrates that the size of S–SnO_2 particles is about 5 nm, and an amorphous shell layer is wrapped around them. The interplanar spacing of ~0.347 nm is characteristic of the (110) plane of SnO_2 (PDF#41-1445). Moreover, the uniform dispersion of C, Sn, O, S, and N elements in the EDS elemental mappings is detected in the S–SnO_2–CFN-2 (Figure 1K). The N, S incorporated in situ into carbon fibers can effectively provide sufficient defects and active sites for sodium/potassium ion storage.

Figure 2A shows XRD patterns of as-prepared samples S–SnO_2–CFN-2 and SnO_2–CFN. All diffraction peaks of the two nanocomposites can be well indexed to the tetragonal phase SnO_2 (JCPDS Card No. 41-1445) with no impurity peaks, indicating high purity.[25] The peaks located at 26.6°, 33.8°, 37.8°, 51.7°, 57.7°, 66°, and 78.8° can be indexed to the (110), (101), (200), (211), (220), (301), and (312) faces of SnO_2, respectively. The XRD peak at (110) for S–SnO_2–CFN-2 slightly shifted to a low degree after sulfur doping, indicating an expanded d-spacing of the crystal face which can facilitate ion insertion and extraction, as displayed in Figure 2B.[26] Moreover, the phases of pure SnO_2 and other S–SnO_2–CFNs were also characterized, as shown in Figure S3. The XRD patterns of pure SnO_2 and other S–SnO_2–CFN-3 can be well matched with the tetragonal

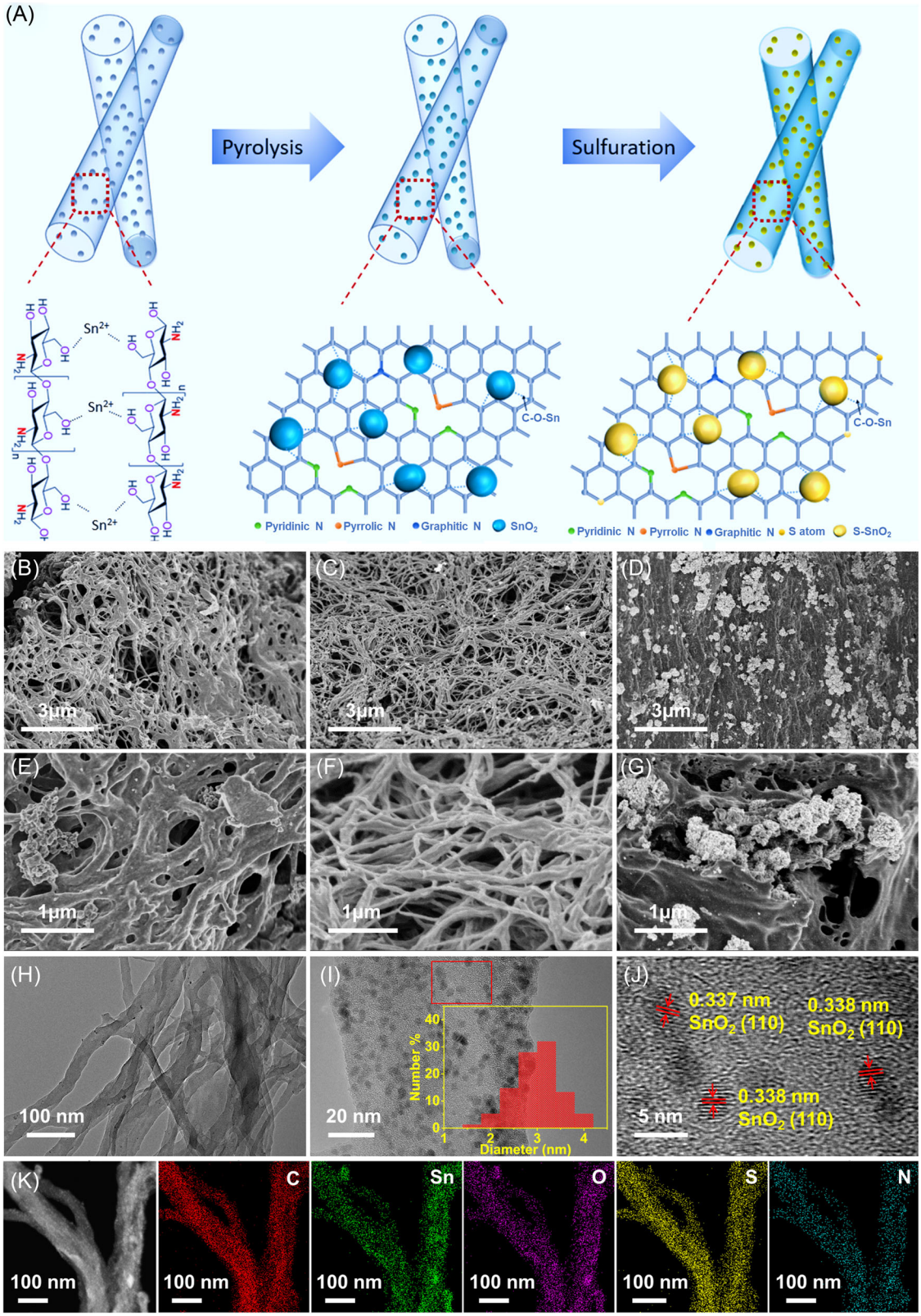

FIGURE 1 (A) Schematic of the preparation process of S–SnO_2–CFN composites. SEM images of (B, E) S–SnO_2–CFN-1, (C, F) S–SnO_2–CFN-2, and (D, G) S–SnO_2–CFN-3 composites. (H, I) TEM, (J) HRTEM (selected area shown in Panel I), and (K) STEM-EDS mapping images of S–SnO_2–CFN-2 composite. Size distribution is inserted in Panel I. CFN, carbon fiber networks.

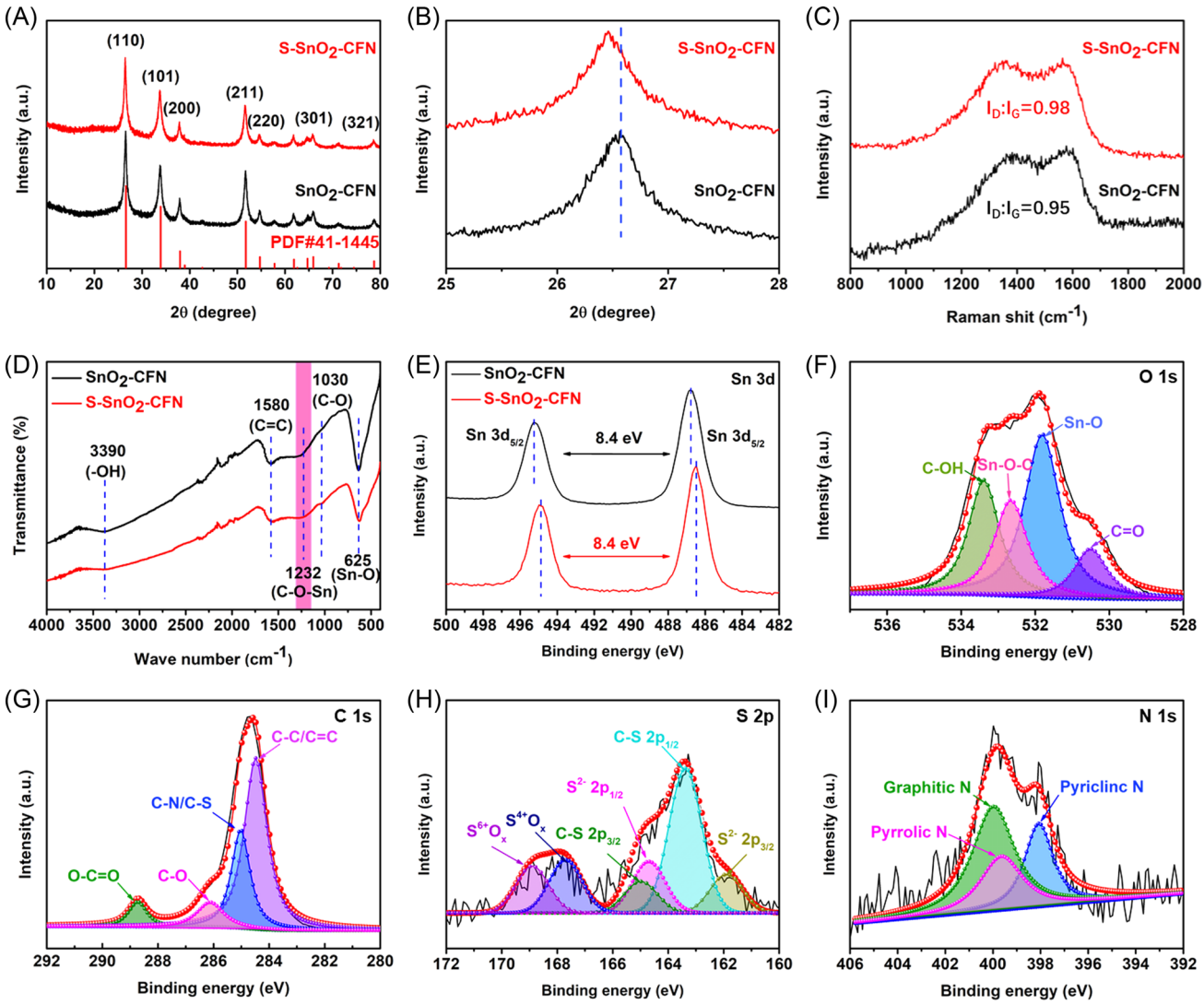

FIGURE 2 (A, B) XRD patterns, (C) Raman spectra, (D) FTIR spectra, and (E) Sn 3d XPS spectra of S–SnO_2–CFN-2 and SnO_2–CFN-2 composites; (F) O 1s, (G) C 1s, (H) S 2p, and (I) N 1s XPS spectra of S–SnO_2–CFN-2. CFN, carbon fiber networks.

phase SnO_2. However, for the S–SnO_2–CFN-1, it was observed that two impurity peaks appeared at 15.1° and 31.9°. This indicates that the amount of chitosan used could impact the morphology and composition of the final product.[27]

Figure 2C illustrates the Raman spectra of S–SnO_2–CFN-2 and SnO_2–CFN, in which defect or disorder-induced D band and the first-order graphite G band were seen at about 1590 cm^{-1} and 1360 cm^{-1}, respectively.[28] The intensity ratio of the D band and G band (I_D/I_G) bands was increased from 0.95 to 0.98 after S doping. In general, the intensity ratio of the D and G bands has been widely used to obtain a quantitative analysis of graphene materials: the higher the ratio, the higher the disorder.[29] Thus, the more defects of carbon fiber in the S–SnO_2–CFN-2 composite will provide more active sites for Na/K ions adsorption, leading to better electrochemical performance. Moreover, the chemical bond between carbon and SnO_2 was further demonstrated by FTIR (Figure 2D). The strong Sn–O–C covalent bonds (1232 cm^{-1}) between SnO_2 QDs and CFNs enable SnO_2 QDs to anchor tightly into the conductive carbon skeleton, which is conducive to improving structural stability and electrochemical performance.[30,31] Besides, other functional groups are also observed, such as OH (3390 cm^{-1}), C=C (1580 cm^{-1}), C–O (1030 cm^{-1}), and Sn–O (625 cm^{-1}) groups.[32] Moreover, an XPS test was conducted to verify the chemical and valence state. The survey XPS spectrum in Figure S4 shows that the S–SnO_2–CFN-2 contains C, Sn, O, N, and S elements. Figure 2E compares the Sn 3d spectra of SnO_2–CFN-2. It can be seen that the binding energy of Sn 3d shifted to a lower binding energy after S doping, which would be beneficial for the electrochemical reaction.[6] Note that the

difference in binding energies of the two Sn oxidation states for the two samples is 8.4 eV, which was consistent with the literature. Figure 2F–I shows high-resolution XPS spectra of O 1s, C 1s, S 2p, and N 1s for the S–SnO_2–CFN-2 composite. The O 1s peak (Figure 2F) could be deconvoluted into four subpeaks, which can be assigned to C=O (530.4 eV), Sn–O (531.7 eV), Sn–O–C (532.6 eV), and C–OH/C–O–C (533.4 eV), respectively.[33,34] The existence of the Sn–O–C bond is consistent with the result of the FTIR measurement. Sn-O-C bond can not only efficiently accelerate electron transport and ion transfer but also effectively prevent the aggregation of Sn particles during cycling. In the high-resolution C 1s XPS spectrum (Figure 2G), four peaks can be observed. The remarkable peak at 284.5 eV should be assigned to the C–C/C=C bond.[35] The other three peaks located at 288.7, 286.1, and 285.0 eV correspond to the O–C=O, C–O, and C–N/C–S bonds, respectively.[36] The S 2p core level spectrum (Figure 2H) can be split into four spin-orbit doublets: S^{2-} $2p_{3/2}$ (161.9 eV), C–S $2p_{1/2}$ (163.4 eV), S^{2-} $2p_{1/2}$ (164.68 eV), and C–S $2p_{3/2}$ (164.98 eV), indicating the existence of C–S bond and S^{2-}.[37] In addition, the presence of the SO_x bonds may be related to their surface oxidation state.[38] Moreover, the carbon materials without Sn (S-carbon) composite and sulfur-doped SnO_2 without carbon (S–SnO_2) composite were prepared, and the S 2p XPS spectra of the S-carbon and S–SnO_2 were measured, as shown in Figure S5. Additionally, ICP results showed that the amount of S doping in the S–SnO_2–CFN-2 composite was ~6.1%. The N 1s spectrum (Figure 2I) contains three peaks at around 398.2, 399.58, and 400.0 eV corresponding to pyridinic N, pyrrolic N, and graphitic N, respectively, indicating that N doping can be introduced from chitosan.[39 40,41] The introduction of N and S is expected to not only generate defects to reserve more Na^+/K^+ ions but also strengthen ion reaction kinetics by improving the conductivity of the S–SnO_2–CFN composite.[42] Moreover, to obtain the weight percentage of SnO_2 in S–SnO_2–CFN-2, thermogravimetric analysis (TGA) was carried out with samples in N_2 flow, and the resulting profile was presented in Figure S6. The initial weight loss (~1.55%) was attributed to the evaporation of the absorbed water. The following weight loss (~21.30%) was attributed to the evaporation of carbon. Therefore, based on the TGA data, the weight ratio of SnO_2 and carbon in the composite was 21.62% and 78.38%, respectively.

The electrochemical performance of S–SnO_2–CFN composites as anodes for SIBs was investigated by using a half-cell at a voltage window of 0.01–3 V. Figure 3A exhibits the CV of S–SnO_2–CFN-2 for the first three cycles. The initial cathodic scan curve exhibits a slightly dissimilar profile compared to the second and third scans, which may be attributed to the formation of the SEI layer and side reactions.[43] The additional cathodic peaks observed in the potential region ranging from 0.80 to 0.01 V are attributed to the formation of amorphous Na_xSn and subsequently crystalline $Na_{15}Sn_4$ ($Sn + xNa^+ + xe^- \rightarrow Na_xSn$).[44] During the anodic scan, the broad oxidation peak ranging from 0.01 to 2.0 V can be attributed to the dealloying phenomenon (of Na_xSn) that results in the formation of Sn.[45] Subsequent CV scans exhibited significant overlap of the CV curves, which is indicative of excellent stability and reversibility of the system. Figure 3B illustrates the GDC curves of S–SnO_2–CFN-2 at a current density of 0.1 A g^{-1}. The material displayed an initial discharge capacity of 906.3 mAh g^{-1} and an initial charge capacity of 609.1 mAh g^{-1}, resulting in an initial Coulombic efficiency (ICE) of up to 67.1%. The observed capacity loss during the first cycle is attributed to the formation of the SEI film and side reactions, consistent with the findings of the CV experiments. The rate performance of S–SnO_2–CFN-2 was evaluated by varying the current densities from 0.1 to 20 A g^{-1}, as shown in Figure 3C. The material exhibited excellent rate capability, delivering discharge capacities of 639.5, 540.7, 453.1, 404.6, 343.2, and 266.1 mAh g^{-1} as the current density increased from 0.1 to 0.2, 0.5, 1, 2, and 5 A g^{-1}, respectively. Furthermore, high specific capacities of 203.0 and 141.0 mAh g^{-1} were achieved even at high current densities of 10 and 20 A g^{-1}, respectively, which significantly outperformed those of S–SnO_2–CFN-1, S–SnO_2–CFN-3, SnO_2–CFN-2, and pure SnO_2 (Table S1). Even after cycling at 20 A g^{-1} for five cycles, a high capacity of 532.8 mAh g^{-1} was recovered at 0.1 A g^{-1}, retaining 83% of the initial capacity delivered at the same current density. These results demonstrate the great potential of S–SnO_2–CFN-2 as an anode material in SIBs. Notably, pure SnO_2 nanoparticles exhibited the lowest rate capacity compared with other materials, indicating that carbon modification can significantly enhance the rate capability. Furthermore, a direct comparison of the rate capacities of S–SnO_2–CFN-2 and SnO_2–CFN-2 reveals that S doping significantly enhances the rate performance. The GDC profiles of S–SnO_2–CFN-2 at various current densities from 0.1 to 20 A g^{-1} are depicted in Figure 3D, and they demonstrate excellent stability and negligible capacity fade with increasing current density. This may be attributed to the enhancement of electrical conductivity due to sulfur doping. Additionally, the electrochemical impedance spectroscopy test has also confirmed this point (Figure S7). The cycle performance of the S–SnO_2–CFN-2 was investigated by GDC measurement. As displayed in Figure 3E, the SnO_2, S–SnO_2–CFN-1, S–SnO_2–CFN-3, SnO_2–CFN-2, and S–SnO_2–CFN-2 electrodes all show excellent cycling stability at 0.2 A g^{-1}. The electrode

composed of S–SnO_2–CFN-2 exhibits the most desirable capacity, delivering a high reversible capacity of 466.6 mAh g^{-1} after 150 cycles, surpassing the capacities of SnO_2 (89.1 mAh g^{-1}), S–SnO_2–CFN-1 (368.7 mAh g^{-1}), S–SnO_2–CFN-3 (335.9 mAh g^{-1}), and SnO_2–CFN-2 (310.1 mAh g^{-1}). Even after 200 cycles, the S–SnO_2–CFN-2 electrode still maintains a high reversible capacity of 459.5 mAh g^{-1}, indicating its excellent cycling

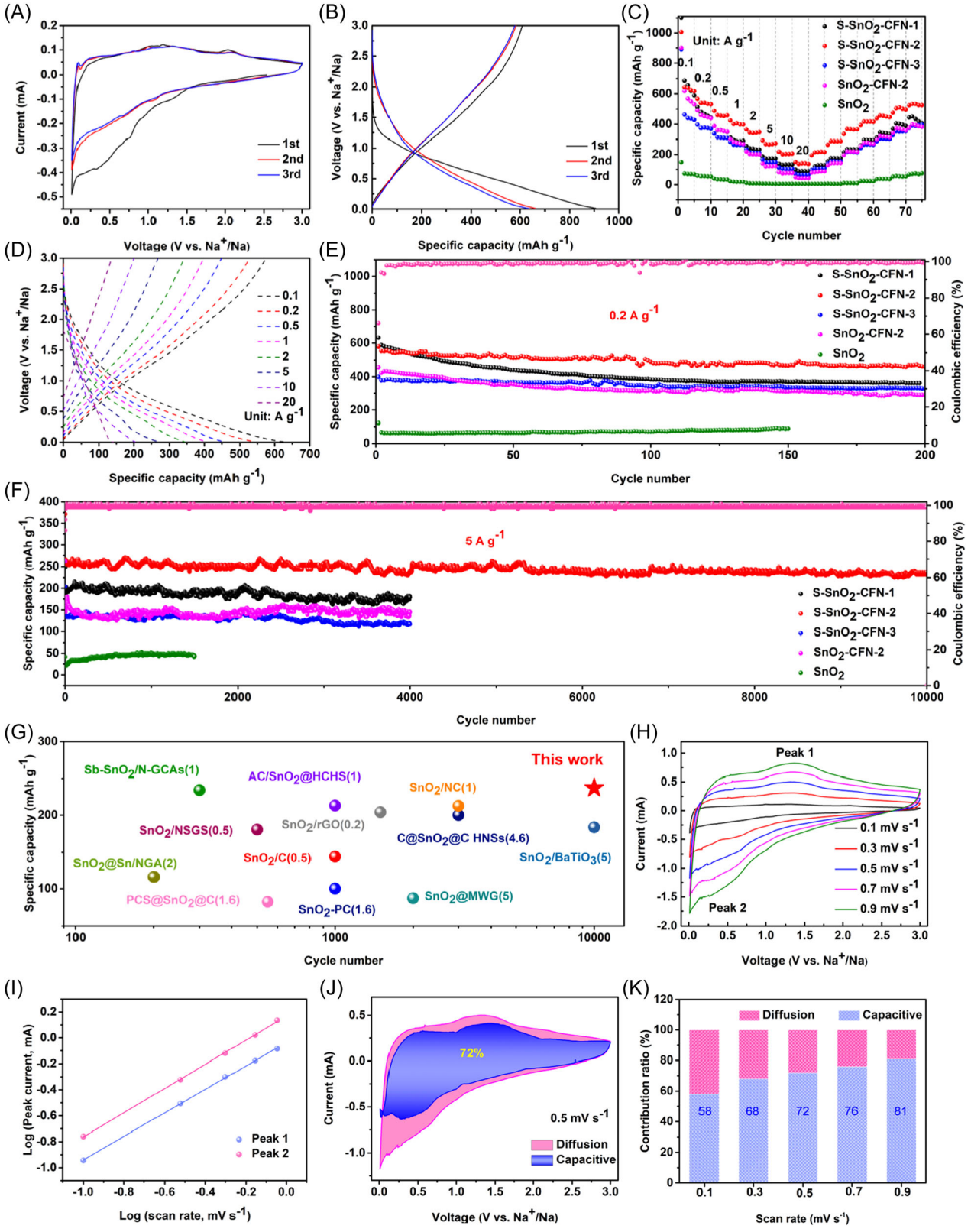

FIGURE 3 (See caption on next page).

stability and potential for practical application in SIBs. To assess its long-term cycling stability under high-rate conditions, the performance of SnO_2–CFN-2 was investigated at a high current density of 5 A g^{-1}, as presented in Figure 3F. Remarkably, the S–SnO_2–CFN-2 electrode exhibited excellent capacity retention and demonstrated an exceptionally long cycle life of up to 10,000 cycles (237.0 mAh g^{-1}) without any noticeable capacity degradation. To further comprehend the exceptional electrochemical properties of the S–SnO_2–CFN-2 electrode, ex situ TEM was carried out, as shown in Figure S8. It can be seen that the fiber structures were well preserved during the discharge and charge process. Besides, the morphology was also analyzed using SEM after 300 cycles at 5.0 A g^{-1}, as illustrated in Figure S9. The fiber network structure was found to be well-preserved even after cycling, indicating superior structural stability, while the pure SnO_2 particles without carbon modification suffered from serious aggregation after 300 cycles at 5.0 A g^{-1} (Figure S10). This can be attributed to the repeated expansion and contraction of the particles during charge and discharge cycles, which leads to structural instability and a loss of cohesion between neighboring particles. This aggregation can result in a decline in electrode performance, including decreased capacity and lower cycling stability. The outcome reveals that the distinct carbon configuration effectively hinders the pulverization and clustering of SnO_2 particles, thereby preserving the structural soundness and steadiness of the entire electrode, which, in turn, guarantees extended cycling endurance. Such exceptional electrochemical performance of S–SnO_2–CFN-2 in SIBs is one of the best outcomes reported in the current literature for carbon fiber structures and tin oxide-based composites (Figure 3G).[18,30,34,46–54] In comparison to typical sodium ion storage systems that display lower capacity and less favorable cyclability under moderate current densities, the S–SnO_2–CFN-2 composite demonstrated exceptional cyclability and capacity due to its optimized structure that incorporates S–SnO_2 QDs and N, S codoped carbon framework.

To provide further elucidation on the reaction kinetics of the S–SnO_2–CFN-2 electrode, CV measurements were conducted at various scanning rates ranging from 0.1 to 0.9 mV s^{-1} (Figure 3H). The results reveal that the CV curves exhibit consistent profiles across different scanning rates, which suggests a typical pseudocapacitance behavior. The peak current (i) and sweep rate (v) obey the following equation[55]:

$$i = av^b, \tag{1}$$

$$\log(i) = b\log(v) + \log(a), \tag{2}$$

where a and b are parameters. It should be noted that the value of b can be derived from the slopes of the curves described in Equation (2), which are plotted by logarithmically scaling the peak current ($\log(i)$) against the logarithmically scaled scan rate ($\log(v)$). The Na^+ storage mechanism can then be discerned based on the resulting value of b: b value of 0.5 indicates that the charge–discharge process is governed by the diffusion mechanism, whereas b value of 1.0 implies a pseudocapacitive behavior.[56] The calculated b values (Figure 3I) for Peak 1 and Peak 2 are roughly 0.90 and 0.93, respectively, suggesting a significant presence of Faradaic pseudocapacitance in the kinetics of each peak, coupled with a diffusion-controlled mechanism. The contributions of the capacitance effect (k_1v) and the ion-diffusion process ($k_2v^{1/2}$) to the current can be determined at a constant scan rate using the following equation[57]:

$$i(v) = k_1v + k_2v^{1/2}, \tag{3}$$

where k_1 and k_2 are constants. Figure 3J illustrates that 72% of the capacitive contribution arises from pseudocapacitive processes at the rate of 0.5 mV s^{-1}. Moreover, it was observed that the capacitance contribution rates exhibited a gradual rise from 58%, 68%, 72%, 76%, and 81% with the escalation of scan rates from 0.1, 0.3, 0.5, 0.7, and 0.9 mV s^{-1}, respectively, as depicted in Figure 3K. This trend indicates that the capacitive-controlled process overwhelmingly governs the Na^+ storage capacity in S–SnO_2–CFN-2. Such a high capacitive contribution could be ascribed to the synergistic

FIGURE 3 Electrochemical sodium storage performances of S–SnO_2–CFN, SnO_2–CFN-2, and pure SnO_2 anodes. (A) CV curves of S–SnO_2–CFN-2 at a scan rate of 0.1 mV s^{-1} in a potential range of 0.01–3.0 V. (B) GDC profiles of S–SnO_2–CFN-2 at a current density of 0.1 A g^{-1}. (C) Rate performance of S–SnO_2–CFN, SnO_2–CFN-2, and pure SnO_2 anodes with current densities ranging from 0.1 to 20 A g^{-1}. (D) Charge and discharge profiles at current densities ranging from 0.1 to 20 A g^{-1}. (E) Cycling performance of S–SnO_2–CFN, SnO_2–CFN-2, and pure SnO_2 anodes at a current density of 0.2 A g^{-1}. (F) Cycling performance of S–SnO_2–CFN, SnO_2–CFN-2, and pure SnO_2 anodes at a current density of 5 A g^{-1}. (G) Comparison of cycling performance between S–SnO_2–CFN-2 and other representative SnO_2-based anodes for SIBs. (H) CV curves of S–SnO_2–CFN-2 under various sweep rates from 0.1 to 0.9 mV s^{-1}. (I) b Values calculated according to the slope of fitted $\log(i)$ against $\log(v)$ plots. (J) The capacitive and diffusive contributions of the S–SnO_2–CFN-2 composite at 0.5 mV s^{-1}. (K) The capacitive contribution ratio at different scan rates for the S–SnO_2–CFN-2 composite. CFN, carbon fiber networks.

effect of S–SnO_2 QDs and N, S codoped carbon fiber network which can provide rough surfaces, plentiful contact areas, and high conductivity and thus facilitate fast charge storage and, consequently, yields superior rate capability.

Motivated by the exceptional sodium ion storage capabilities, the electrochemical behavior of the S–SnO_2–CFN-2 composite in potassium half-cells was investigated at a voltage range of 0.01–3.0 V. The first three cycles of the S–SnO_2–CFN-2 composite were evaluated through CV at a scanning rate of 0.1 mV s^{-1}, as presented in Figure 4A. The initial CV curve profile differed from the subsequent two curves, which could be attributed to the formation of SEI film and other irreversible side reactions. However, the CV curves of the second and third cycles exhibited similar profiles, indicating good electrochemical reversibility of the S–SnO_2–CFN-2 composite. During the first cathodic scan, two cathodic peaks are observed at approximately 0.01 and 0.6 V. The peak at 0.6 V is a result of the conversion reaction ($4K^+ + SnO_2 + 4e^- \rightarrow Sn + 2K_2O$), which causes the phase change of SnO_2 to Sn and K^+ to K_2O, and the irreversible reaction that leads to the formation of the SEI and moves to the range of 0.6–1.1 V upon the second cathodic scan.[58] The cathodic peak emerges at a potential around 0.01 V, which can be attributed to the formation of K–Sn alloy ($xK^+ + Sn + xe^- \leftrightarrow K_xSn$) and the intercalation of K ion into the amorphous carbon layer ($xK^+ + C + xe^- \leftrightarrow K_xC$).[59] During the subsequent anodic scan, the broad peak located at ~0.5 V is related to the deintercalation of K ion from amorphous carbon, and a series of minor peaks was detected at 1.02, 1.30, and 1.5 V, which can be attributed to progressive dealloying phenomena.[58] Figure 4B depicts the first three GDC profiles of S–SnO_2–CFN-2 recorded at a current density of 0.1 A g^{-1}. The electrode exhibits an initial discharge capacity of 889 mAh g^{-1}, along with a high reversible charge capacity of 490 mAh g^{-1}, leading to an ICE of 55%. To assess the long-term cycling performance of S–SnO_2–CFN-2, we conducted cycling tests at a current density of 0.2 A g^{-1}, as shown in Figure 4C. The electrode exhibited a high and stable reversible capacity of 394.1 mAh g^{-1} after 100 cycles. In contrast, SnO_2–CFN-2 suffered from severe capacity fading during cycling and showed a low capacity of 97.7 mAh g^{-1} after 100 cycles, while SnO_2 exhibited an even lower reversible capacity, with a capacity of 47.3 mAh g^{-1} after 100 cycles. In addition, the rate capability of S–SnO_2–CFN-2, SnO_2–CFN-2, and SnO_2 was evaluated and displayed in Figure 4D. SnO_2–CFN-2 and SnO_2 exhibited a less desirable rate capability, whereas S–SnO_2–CFN-2 demonstrated exceptional stability at various current densities. Specifically, the discharge capacities achieved at current densities of 0.1, 0.2, 0.5, 1.0, 2.0, and 5 A g^{-1} were 520.8, 423.6, 365.5, 322.4, 269.5, and 162.5 mAh g^{-1}, respectively. Notably, even at a high current density of 10 A g^{-1}, the electrode delivered a capacity higher than 102.8 mAh g^{-1}. Encouraged by the remarkable rate capability, we further evaluated the long-term cycling stability of S–SnO_2–CFN-2 at a higher current density of 2 A g^{-1} using GDC measurement. As depicted in Figure 4E, the specific capacity of S–SnO_2–CFN-2 initially decreased during the first 300 cycles but then recovered to 266 mAh g^{-1} at around the 390th cycle. Subsequently, the capacity remained stable around 145.5 mAh g^{-1} until the 5000th cycle, with a Coulomb efficiency close to 100%. This phenomenon can be attributed to the formation and stabilization process of the SEI. During the initial cycles, the electrode materials, especially tin oxide (SnO_2), can react with the electrolyte components, leading to the formation of an SEI layer on the electrode surface. This SEI layer can impede the flow of sodium ions, resulting in a slight decrease in discharge capacity. However, with continued cycling, the SEI layer may stabilize and become more permeable, allowing improved sodium ion transport and enhancing the discharge capacity. In contrast, SnO_2 and SnO_2–CFN-2 electrodes displayed poor cycling stability, delivering low capacities of 21.2 and 2.3 mAh g^{-1} after 5000 cycles, respectively. The enhanced cycling performance of S–SnO_2–CFN-2 can be attributed to the formation of S-doped SnO_2 and N, S codoped carbon, which can improve ion and electron transport efficiency. To gain insight into the excellent electrochemical properties of the S–SnO_2–CFN-2 electrode, ex situ TEM was carried out, as shown in Figure S11. It can be seen that the fiber structures were well preserved during the discharge and charge process. Besides, we also conducted SEM analysis (Figure S12) on the electrode material after 300 cycles at 2.0 A g^{-1}. The analysis revealed that the carbon fiber network structure remained intact even after repeated charge and discharge cycles, indicating a high degree of structural stability, while the pure SnO_2 particles without carbon modification suffered from serious aggregation after 300 cycles at 2.0 A g^{-1} (Figure S13). The electrochemical performance of the S–SnO_2–CFN-2 electrode in PIBs was found to be one of the best among SnO_2-based composites in existing literature (Figure 4F).[11,13,49,58–67] These findings suggest that the S–SnO_2–CFN-2 electrode has significant potential as an anode material in PIBs.

To investigate the exceptional rate performance of the material, we calculated the contribution of capacitance based on CV measurements conducted at different scan rates. Figure 4G shows the CV curves obtained at scan rates ranging from 0.1 to 0.9 mV s^{-1}, which exhibited

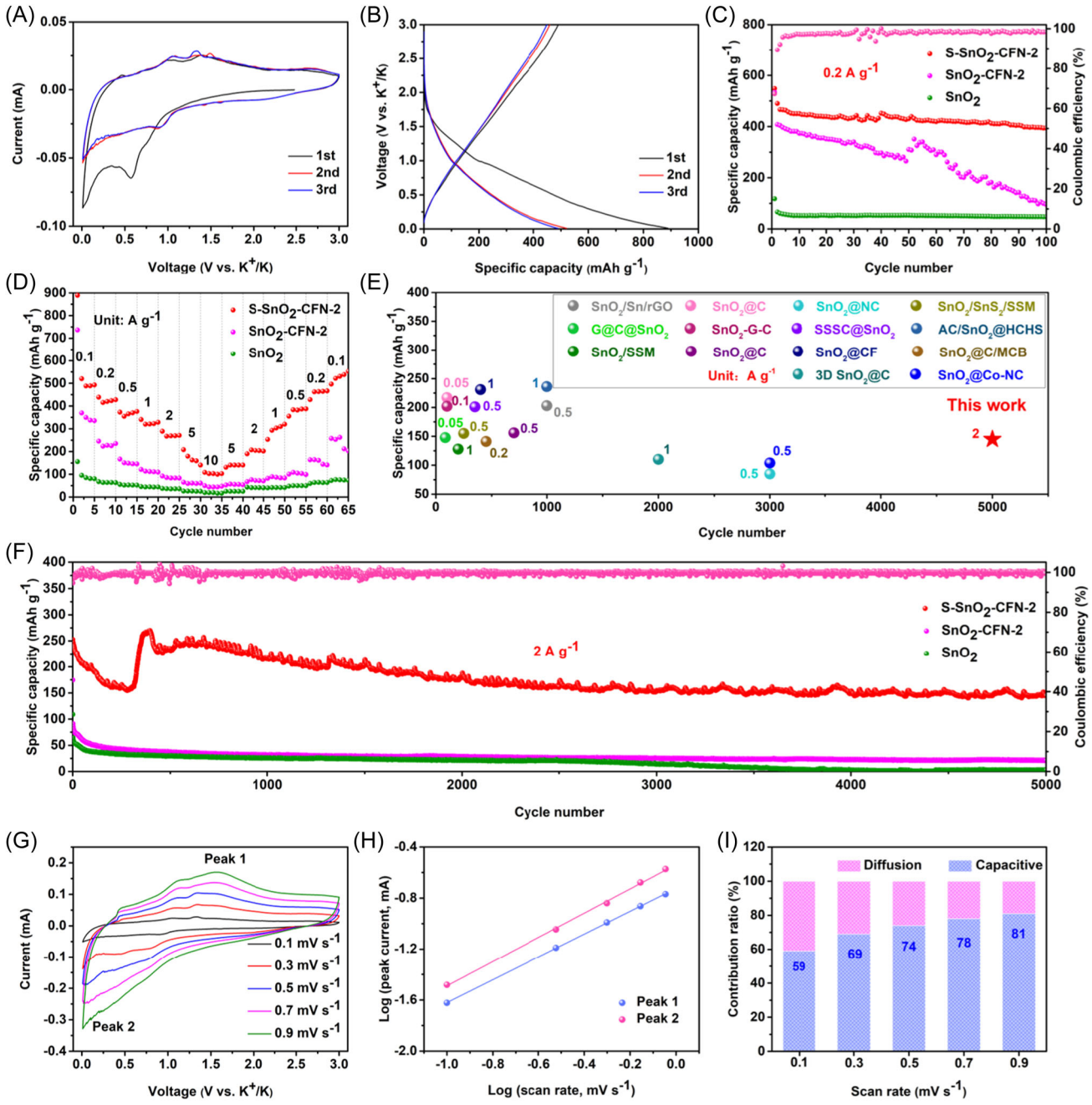

FIGURE 4 Electrochemical potassium storage performances of S–SnO_2–CFN-2 SnO_2–CFN-2, and pure SnO_2 anodes. (A) CV curves of S–SnO_2–CFN-2 at a scan rate of 0.1 mV s^{-1} in a potential range of 0.01–3.0 V. (B) GDC profiles of S–SnO_2–CFN-2 at a current density of 0.1 A g^{-1}. (C) Cycling performance of S–SnO_2–CFN-2, SnO_2–CFN-2, and pure SnO_2 anodes at a current density of 0.2 A g^{-1}. (D) Rate performance of S–SnO_2–CFN-2, SnO_2–CFN-2, and pure SnO_2 anodes with current densities ranging from 0.1 to 10 A g^{-1}. (E) Cycling performance of S–SnO_2–CFN-2, SnO_2–CFN-2, and pure SnO_2 anodes at a current density of 2 A g^{-1}. (F) Comparison of cycling performance between S–SnO_2–CFN-2 and other representative SnO_2-based anodes for PIBs. (G) CV curves of S–SnO_2–CFN-2 under various sweep rates from 0.1 to 0.9 mV s^{-1}. (H) *b* Values calculated according to the slope of fitted log(*i*) against log(*v*) plots. (I) The capacitive contribution ratio at different scan rates for the S–SnO_2–CFN-2 composite. CFN, carbon fiber networks.

similar profiles and minimal polarization. The calculated *b* values (Figure 4H) for Peak 1 and Peak 2 are roughly 0.89 and 0.95, respectively, suggesting a significant presence of Faradaic pseudocapacitance in the kinetics of each peak, coupled with a diffusion-controlled mechanism. A representative CV curve obtained at a scan rate of 0.5 mV s^{-1} is shown in Figure S14, with a calculated capacitive contribution of 74%. Figure 4I illustrates that the capacitance contribution ratios increased from 59% to 81% with an increase in scan rate

from 0.1 to 0.9 mV s^{-1}. These results suggest that the exceptional rate performance of the material can be attributed to its high capacitance contribution, which increases with scan rate. Additionally, the structural stability of electrode materials during discharge and charge is a crucial factor in determining their electrochemical performance.

DFT calculations were implemented to gain further insight into the extraordinary electrochemical performance of the S–SnO_2–CFN anode. The adsorption energies (E_{ads}) were employed to compare the energy change. As present in Figure 5A–D, the E_{ads} values of Na/K atoms with S–SnO_2–CFN and SnO_2 were calculated to be −0.51/−1.47 eV, and −0.40/−1.39 eV, respectively, suggesting stronger interaction between the Na/K atom and S–SnO_2–CFN. Figure 5E–H displays the charge density differences of SnO_2 and S–SnO_2–CFN systems, in which the charge accumulation region (green parts) and charge depletion region (blue parts) showed the charge transfer from the Na/K atom to the samples. In the S–SnO_2–CFN system, the charge accumulation regions exist not only between the Na/K atom and S–SnO_2 but also between the Na/K atom and carbon layers. Note that the charge accumulated around N and S atoms in the carbon layer was observed, indicating partial charge transfer from Na/K to N and S. Moreover, the charge accumulation regions around the S–SnO_2–CFN interface are larger than that of pure SnO_2 surfaces, suggesting the strong binding energy between the Na/K atom and S–SnO_2–CFN. These results indicate that the N, S codoped carbon modification can

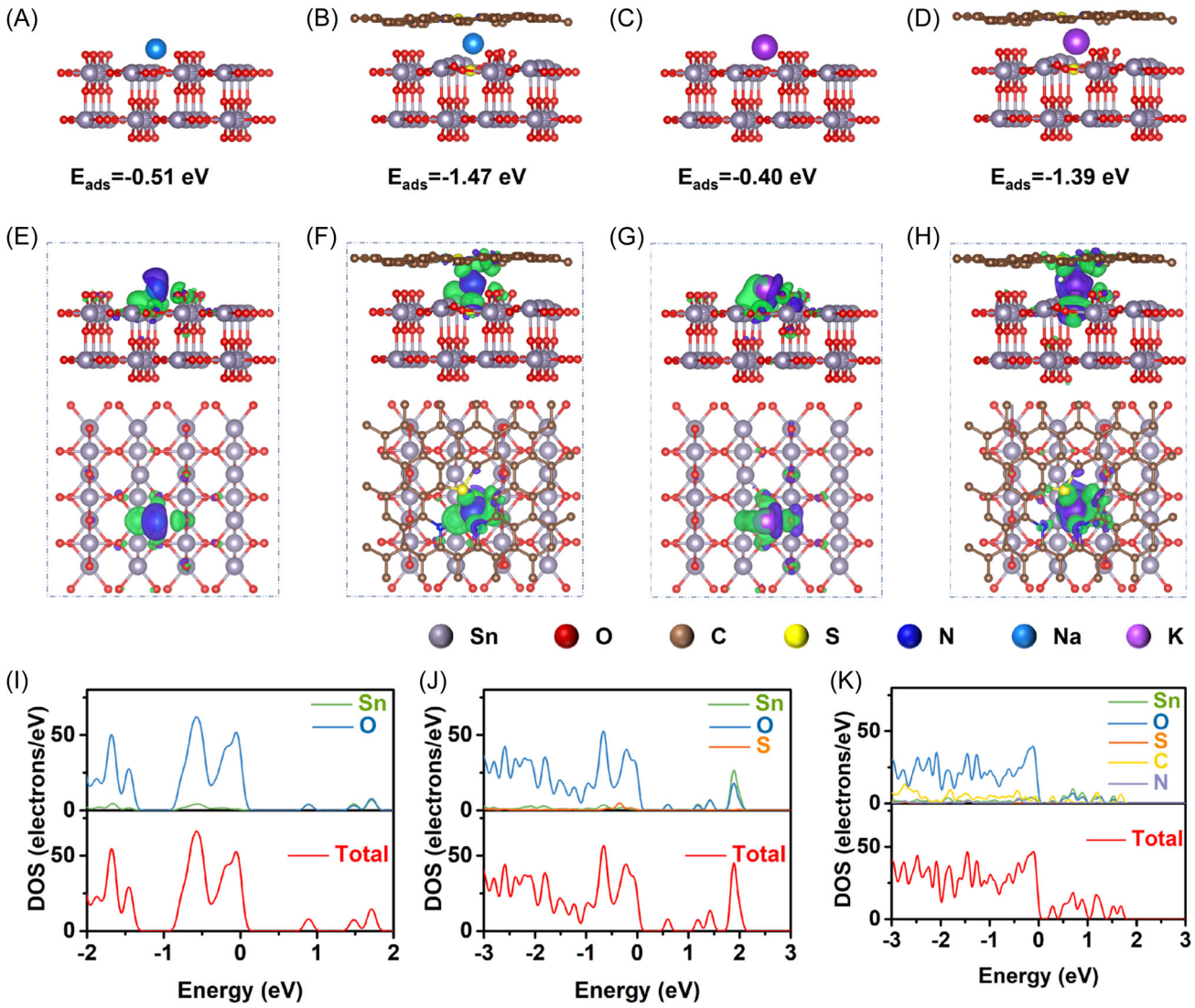

FIGURE 5 The DFT calculation models with a Na or K atom adsorbed on (A, C) SnO_2 and (B, D) S–SnO_2–CFN composite. The corresponding adsorption energies are presented under the model. Charge density differences with a Na or K atom adsorbed on (E, G) SnO_2 and (F, H) S–SnO_2–CFN composite (top view and side view), green region and blue region represent the charge accumulation and loss, respectively. DOS of SnO_2(110) surface before (I) and after (J) S doping. (K) DOS of S-SnO_2-CFN. CFN, carbon fiber networks.

strengthen the Na/K atom adsorption ability of S–SnO_2, thus enhancing ion storage capacity. Additionally, the density of states (DOS) of SnO_2 and S–SnO_2 are calculated to discuss their electrical properties. Figure 5I illustrates the DOS of pure SnO_2, where the valence band primarily comprises O 2p states. Within the conduction band, four distinct regions can be identified where the contribution from Sn 2p and O 2p states are comparable. The band gap of SnO_2 is approximately 0.900 eV. Figure 5J depicts the DOS of S–SnO_2. The plot reveals a downward shift in the DOS, the emergence of new doping levels near the Fermi level, and a reduction in the nanoparticle's band gap from 0.900 eV (pure SnO_2) to 0.59 eV (S–SnO_2). Consequently, S doping can enhance the conductivity properties of SnO_2 by facilitating electron transfer from the top to the bottom of the valence band. Moreover, the S–SnO_2–CFN composite manifests conductive properties, as evidenced by Figures 5K and S15. The computational results reveal that adding an N, S codoped carbon layer and S doping can significantly enhance the ion adsorption ability and electrical conductivity of SnO_2 anodes. As a result, S–SnO_2–CFN exhibits significantly improved electrochemical performance in both SIBs and PIBs compared to pure SnO_2 anodes.

4 | CONCLUSION

In conclusion, S–SnO_2 QDs (≈3 nm) encapsulated in N, S codoped carbon fiber network are successfully synthesized using a simple freezing-dry method followed by the carbonization and S-doping process. The introduction of S–SnO_2 QDs can offer several advantages, including the reduction of absolute volume change, the decrease of ion diffusion length, and the improvement of electrical conductivity. Moreover, compared to Sn–O bonds in SnO_2, the relatively weaker Sn–S bonds in S–SnO_2 QDs benefit the insertion and extraction of Na^+/K^+ ions. The N, S codoped carbon fiber network structure can enhance electronic conductivity, provide numerous active sites and electron/ion transport channels, and create internal void spaces between fibers to accommodate volume expansion. DFT calculations further confirmed that the integration of SnO_2 with N, S codoped carbon fiber network can significantly lower the adsorbed energies of Na/K atoms in the interlayer of SnO_2-CFN, and S doping can increase the conductivity of SnO_2, thereby enhancing ion transfer kinetics. As SIB's anode, the S–SnO_2–CFN-2 composite exhibited a maintainable capacity (237.0 mAh g^{-1} at 5 A g^{-1} upon 10,000 cycles) and outstanding rate behavior (141.0 mAh g^{-1} at 20 A g^{-1}). As PIB's anode, the S–SnO_2–CFN-2 composite also exhibited a maintainable capacity (145.5 mAh g^{-1} at 2 A g^{-1} upon 5000 cycles) and remarkable rate capability (102.8 mAh g^{-1} at 10 A g^{-1}). The excellent electrochemical performance could be assigned to the synergistic effect of S–SnO_2 QDs and N, S codoped carbon framework, which could effectively prevent the aggregation and pulverization of SnO_2 QDs, ensure structural stability, enhance electronic–ionic conductivity, and offer large contact area between active materials and electrolytes. Our synthetic protocol proposed here may be potentially used for fabricating novel metal oxide-based nanostructures and nanocomposites for SIBs/PIBs.

ACKNOWLEDGMENTS

This work is supported by the National Natural Science Foundation of China (Grant No. 51971065) and the Innovation Program of Shanghai Municipal Education Commission (2019-01-07-00-07-E00028). The authors would like to thank SCI-GO (www.sci-go.com) for the transmission electron microscopy analysis.

CONFLICT OF INTEREST STATEMENT

The authors declare that there are no conflict of interests.

ORCID

Xuebin Yu https://orcid.org/0000-0002-4035-0991

REFERENCES

1. Li M, Lu J, Chen Z, Amine K. 30 Years of lithium-ion batteries. *Adv Mater*. 2018;30(33):1800561.
2. Kim T, Song W, Son DY, Ono LK, Qi Y. Lithium-ion batteries: outlook on present, future, and hybridized technologies. *J Mater Chem A*. 2019;7(7):2942-2964.
3. Choi JW, Aurbach D. Promise and reality of post-lithium-ion batteries with high energy densities. *Nat Rev Mater*. 2016;1(4):16013.
4. Masias A, Marcicki J, Paxton WA. Opportunities and challenges of lithium ion batteries in automotive applications. *ACS Energy Lett*. 2021;6(2):621-630.
5. Hong Z, Maleki H, Ludwig T, et al. New insights into carbon-based and MXene anodes for Na and K-ion storage: a review. *J Energy Chem*. 2021;62:660-691.
6. Song K, Liu C, Mi L, Chou S, Chen W, Shen C. Recent progress on the alloy-based anode for sodium-ion batteries and potassium-ion batteries. *Small*. 2021;17(9):1903194.
7. Wu H, Xiong Z, Mao Y, et al. MoS_2/MoO_2 nanosheets anchored on carbon cloth for high-performance magnesium- and sodium-ion storage. *J Mater Sci Technol*. 2023;143:43-53.
8. Gu Y, Ru Pei Y, Zhao M, Cheng Yang C, Jiang Q. Sn-, Sb-and Bi-based anodes for potassium ion battery. *Chem Rec*. 2022;22(10):e202200098.
9. Li J, Guo C, Li CM. Recent advances of two-dimensional (2D) MXenes and phosphorene for high-performance rechargeable batteries. *ChemSusChem*. 2020;13(6):1047-1070.
10. Wu H, Xia G, Yu X. Recent progress on nanostructured iron-based anodes beyond metal-organic frameworks for sodium-ion batteries. *EnergyChem*. 2023;5(1):100095.

11. Qiu H, Zhao L, Asif M, et al. SnO_2 nanoparticles anchored on carbon foam as a freestanding anode for high performance potassium-ion batteries. *Energy Environ Sci*. 2020;13(2):571-578.
12. Wang M, Wang X, Yao Z, et al. SnO_2 nanoflake arrays coated with polypyrrole on a carbon cloth as flexible anodes for sodium-ion batteries. *ACS Appl Mater Interfaces*. 2019;11(27):24198-24204.
13. Luo S, Wang T, Lu H, et al. Ultrasmall SnO_2 nanocrystals embedded in porous carbon as potassium ion battery anodes with long-term cycling performance. *New J Chem*. 2020;44(27):11678-11683.
14. Zheng Y, Zhou T, Zhang C, Mao J, Liu H, Guo Z. Boosted charge transfer in SnS/SnO_2 heterostructures: toward high rate capability for sodium-ion batteries. *Angew Chem Int Ed*. 2016;55(10):3408-3413.
15. Ma D, Li Y, Mi H, et al. Robust SnO_{2-x} nanoparticle-impregnated carbon nanofibers with outstanding electrochemical performance for advanced sodium-ion batteries. *Angew Chem*. 2018;130(29):9039-9043.
16. Alsamet MAMM, Burgaz E. Synthesis and characterization of nano-sized $LiFePO_4$ by using consecutive combination of sol-gel and hydrothermal methods. *Electrochim Acta*. 2021;367:137530.
17. Han F, Li D, Li WC, Lei C, Sun Q, Lu AH. Nanoengineered polypyrrole-coated Fe_2O_3@C multifunctional composites with an improved cycle stability as lithium-ion anodes. *Adv Funct Mater*. 2013;23(13):1692-1700.
18. Cui J, Yao S, Huang JQ, et al. Sb-doped SnO_2/graphene-CNT aerogels for high performance Li-ion and Na-ion battery anodes. *Energy Storage Mater*. 2017;9:85-95.
19. Liu Y, Hu X, Zhong G, Chen J, Zhan H, Wen Z. Layer-by-layer stacked nanohybrids of N, S-co-doped carbon film modified atomic MoS_2 nanosheets for advanced sodium dual-ion batteries. *J Mater Chem A*. 2019;7(42):24271-24280.
20. Kresse G, Furthmüller J. Efficient iterative schemes for ab initio total-energy calculations using a plane-wave basis set. *Phys Rev B*. 1996;54(16):11169-11186.
21. Kresse G, Furthmüller J. Efficiency of ab-initio total energy calculations for metals and semiconductors using a plane-wave basis set. *Comput Mater Sci*. 1996;6(1):15-50.
22. Perdew JP, Burke K, Ernzerhof M. Generalized gradient approximation made simple. *Phys Rev Lett*. 1996;77(18):3865-3868.
23. Kresse G, Joubert D. From ultrasoft pseudopotentials to the projector augmented-wave method. *Phys Rev B Condens Matter Mater Phys*. 1999;59(3):1758-1775.
24. Blöchl PE. Projector augmented-wave method. *Phys Rev B*. 1994;50(24):17953-17979.
25. Wang Y, Su D, Wang C, Wang G. SnO_2@MWCNT nanocomposite as a high capacity anode material for sodium-ion batteries. *Electrochem Commun*. 2013;29:8-11.
26. Cai Y, Liu F, Luo Z, et al. Pilotaxitic $Na_{1.1}V_3O_{7.9}$ nanoribbons/graphene as high-performance sodium ion battery and aqueous zinc ion battery cathode. *Energy Storage Mater*. 2018;13:168-174.
27. Jiang X, Yang X, Zhu Y, Shen J, Fan K, Li C. In situ assembly of graphene sheets-supported SnS_2 nanoplates into 3D macroporous aerogels for high-performance lithium ion batteries. *J Power Sources*. 2013;237:178-186.
28. Marcus B, Fayette L, Mermoux M, Abello L, Lucazeau G. Analysis of the structure of multi-component carbon films by resonant Raman scattering. *J Appl Phys*. 1994;76(6):3463-3470.
29. Jorio A, Ferreira EHM, Moutinho MVO, Stavale F, Achete CA, Capaz RB. Measuring disorder in graphene with the G and D bands. *Phys Status Solidi B Basic Res*. 2010;247(11-12):2980-2982.
30. Li Y, Liu R, Wang C, Zhou Y. Uniform nano-SnO_2/C composite anodes from coal tar pitch for sodium-ion batteries. *Energy Fuels*. 2021;35(10):9029-9037.
31. Huang Z, Gao H, Ju J, Yu J, Kwon YU, Zhao Y. Sycamore-fruit-like SnO_2@C nanocomposites: rational fabrication, highly reversible capacity and superior rate capability anode material for Li storage. *Electrochim Acta*. 2020;331:135297.
32. Li Y, Zhu S, Liu Q, et al. Carbon-coated SnO_2@C with hierarchically porous structures and graphite layers inside for a high-performance lithium-ion battery. *J Mater Chem*. 2012;22(6):2766-2773.
33. Chen Z, Yin D, Zhang M. Sandwich-like MoS_2@SnO_2@C with high capacity and stability for sodium/potassium ion batteries. *Small*. 2018;14(17):1703818.
34. Qin J, Zhao N, Shi C, et al. Sandwiched C@SnO_2@C hollow nanostructures as an ultralong-lifespan high-rate anode material for lithium-ion and sodium-ion batteries. *J Mater Chem A*. 2017;5(22):10946-10956.
35. Tian Q, Chen Y, Sui Z, Chen J, Yang L. The sandwiched buffer zone enables porous SnO_2@C micro-/nanospheres to toward high-performance lithium-ion battery anodes. *Electrochim Acta*. 2020;354:136699.
36. Sridhar V, Park H. Hollow SnO_2@carbon core–shell spheres stabilized on reduced graphene oxide for high-performance sodium-ion batteries. *New J Chem*. 2017;41(2):442-446.
37. Li C, Hou J, Zhang J, et al. Heterostructured NiS_2@SnS_2 hollow spheres as superior high-rate and durable anodes for sodium-ion batteries. *Sci China Chem*. 2022;65(7):1420-1432.
38. Shao Z, Meng H, Sun J, et al. Engineering of amorphous structures and sulfur defects into ultrathin FeS nanosheets to achieve superior electrocatalytic alkaline oxygen evolution. *ACS Appl Mater Interfaces*. 2020;12(46):51846-51853.
39. Xu C, Sun J, Gao L. Controllable synthesis of monodisperse ultrathin SnO_2 nanorods on nitrogen-doped graphene and its ultrahigh lithium storage properties. *Nanoscale*. 2012;4(17):5425-5430.
40. Mao H, Shi L, Song S, et al. N-doped hollow carbon nanosheet supported SnO_2 nanoparticles. *Inorg Chem Front*. 2017;4(10):1742-1747.
41. Qiao M, Meysami SS, Ferrero GA, et al. Low-cost chitosan-derived N-doped carbons boost electrocatalytic activity of multiwall carbon nanotubes. *Adv Funct Mater*. 2018;28(16):1707284.
42. Xiao S, Li X, Li T, Xiang Y, Chen JS. Practical strategies for enhanced performance of anode materials in Na^+/K^+-ion batteries. *J Mater Chem A*. 2021;9(12):7317-7335.
43. Dixon D, Ávila M, Ehrenberg H, Bhaskar A. Difference in electrochemical mechanism of SnO_2 conversion in lithium-ion and sodium-ion batteries: combined in operando and ex situ XAS investigations. *ACS Omega*. 2019;4(6):9731-9738.

44. Kalubarme RS, Lee JY, Park CJ. Carbon encapsulated tin oxide nanocomposites: an efficient anode for high performance sodium-ion batteries. *ACS Appl Mater Interfaces*. 2015;7(31):17226-17237.
45. Gui D, Wei Z, Chen J, et al. Boosting the sodium storage of the 1T/2H MoS_2@ SnO_2 heterostructure via a fast surface redox reaction. *J Mater Chem A*. 2021;9(1):463-471.
46. Huang Z, Hou H, Zou G, et al. 3D porous carbon encapsulated SnO_2 nanocomposite for ultrastable sodium ion batteries. *Electrochim Acta*. 2016;214:156-164.
47. Wang H, Wu Q, Wang Y, et al. Molecular engineering of monodisperse SnO_2 nanocrystals anchored on doped graphene with high-performance lithium/sodium-storage properties in half/full cells. *Adv Energy Mater*. 2019;9(3):1802993.
48. Ma Y, Wang Q, Liu L, et al. Plasma-enabled ternary SnO_2@Sn/nitrogen-doped graphene aerogel anode for sodium-ion batteries. *ChemElectroChem*. 2020;7(6):1358-1364.
49. Li D, Zhang J, Ahmed S, et al. Amorphous carbon coated SnO_2 nanohseets on hard carbon hollow spheres to boost potassium storage with high surface capacitive contributions. *J Colloid Interface Sci*. 2020;574:174-181.
50. Kong Z, Liu X, Wang T, et al. Three-dimensional hollow spheres of porous SnO_2/rGO composite as high-performance anode for sodium ion batteries. *Appl Surf Sci*. 2019;479:198-208.
51. Li R, Zhang G, Wang Y, et al. Fast ion diffusion kinetics based on ferroelectric and piezoelectric effect of SnO_2/$BaTiO_3$ heterostructures for high-rate sodium storage. *Nano Energy*. 2021;90:106591.
52. Li X, Sun X, Gao Z, et al. Fabrication of porous carbon sphere@SnO_2@carbon layer coating composite as high performance anode for sodium-ion batteries. *Appl Surf Sci*. 2018;433:713-722.
53. Sang J, Liu K, Zhang X, et al. Enabling high-performance sodium battery anodes by complete reduction of graphene oxide and cooperative in situ crystallization of ultrafine SnO_2 nanocrystals. *Energy Environ Mater*. 2023;6(3):e12431.
54. Cheng Y, Wang S, Zhou L, et al. SnO_2 quantum dots: rational design to achieve highly reversible conversion reaction and stable capacities for lithium and sodium storage. *Small*. 2020;16(26):2000681.
55. Zhang Z, Liang J, Zhang X, Yang W, Dong X, Jung Y. Dominant pseudocapacitive lithium storage in the carbon-coated ferric oxide nanoparticles (Fe_2O_3@C) towards anode materials for lithium-ion batteries. *Int J Hydrogen Energy*. 2020;45(15):8186-8197.
56. Lin D, Li K, Wang Q, Lyu L, Li B, Zhou L. Rate-independent and ultra-stable low-temperature sodium storage in pseudocapacitive TiO_2 nanowires. *J Mater Chem A*. 2019;7(33):19297-19304.
57. Tian Z, Sun S, Zhao X, Yang M, Xu C. Phoenix tree leaves-derived biomass carbons for sodium-ion batteries. *Funct Mater Lett*. 2018;11(6):1840008.
58. Wang Z, Dong K, Wang D, et al. Ultrafine SnO_2 nanoparticles encapsulated in 3D porous carbon as a high-performance anode material for potassium-ion batteries. *J Power Sources*. 2019;441:227191.
59. Suo G, Li D, Feng L, et al. Construction of SnS_2/SnO_2 heterostructures with enhanced potassium storage performance. *J Mater Sci Technol*. 2020;55:167-172.
60. Wu S, Feng Y, Jiang W, et al. Reduced graphene oxide coated modified SnO_2 forms excellent potassium storage properties. *Ceram Int*. 2023;49(10):15741-15750.
61. Cheng Y, Chen B, Chang L, et al. Electrochemical activation of oxygen atom of SnO_2 to expedite efficient conversion reaction for alkaline-ion (Li^+/Na^+/K^+) storages. *Nano Res*. 2023;16(1):1642-1650.
62. Suo G, Li D, Feng L, Hou X, Yang Y, Wang W. SnO_2 nanosheets grown on stainless steel mesh as a binder free anode for potassium ion batteries. *J Electroanal Chem*. 2019;833:113-118.
63. Hu Z, Wang M, Yang H, Liang C, Yu K. SnO_2 nanosheets grow on sunflower shell carbon sphere used as anode material for high performance lithium-ion and potassium-ion batteries. *Diamond Relat Mater*. 2022;126:109090.
64. Huang Y, Ding S, Xu S, Ma ZF, Wang J, Yuan X. Highly effective solid electrolyte interface on SnO_2@C enabling stable potassium storage performance. *Chem Eng J*. 2022;446:137265.
65. Xu Z, Huang H, Liu C, et al. Micrometer carbon ball-decorated nanowire-structured SnO_2@C composites as an anode for potassium-ion batteries with enhanced performance. *Energy Fuels*. 2022;36(5):2833-2840.
66. Wu Q, Shao Q, Li Q, Duan Q, Li Y, Wang H. Dual carbon-confined SnO_2 hollow nanospheres enabling high performance for the reversible storage of alkali metal ions. *ACS Appl Mater Interfaces*. 2018;10(18):15642-15651.
67. Huang Z, Chen Z, Ding S, Chen C, Zhang M. Enhanced conductivity and properties of SnO_2-graphene-carbon nanofibers for potassium-ion batteries by graphene modification. *Mater Lett*. 2018;219:19-22.

SUPPORTING INFORMATION

Additional supporting information can be found online in the Supporting Information section at the end of this article.

How to cite this article: He S, Wu H, Li S, et al. Small but mighty: empowering sodium/potassium-ion battery performance with S-doped SnO_2 quantum dots embedded in N, S codoped carbon fiber network. *Carbon Energy*. 2024;e486. doi:10.1002/cey2.486